Resonant metal-mesh bandpass filters for the far infrared

D. W. Porterfield, J. L. Hesler, R. Densing, E. R. Mueller, T. W. Crowe, and R. M. Weikle II

The spectral performance of freestanding resonant metal-mesh bandpass filters operating with center frequencies ranging from 585 GHz to 2.1 THz is presented. These filters are made up of a 12-μm-thick copper film with an array of cross-shaped apertures that fill a circular area with a 50-mm diameter. The filters exhibit power transmission in the range 97–100% at their respective center frequencies and stop-band rejection in excess of 18 dB. The theoretically predicted nondiffracting properties of the meshes are experimentally verified through high-resolution beam mapping. Scalability of the filter spectra with mesh dimensions is demonstrated over a wide spectral range. Several modeling methods are considered, and results from the models are shown.

Key words: Mesh filter, resonant filter, frequency-selective surface, EMF method.

Introduction

There are a number of important applications for bandpass filters in the far-infrared (submillimeter wave) spectrum. For example, superconductor–insulator–superconductor tunnel junction mixers require bandpass filtering to avoid saturation by thermal radiation. In addition, one may reduce the noise equivalent power of a cooled bolometer by using a cooled bandpass filter to block thermal radiation over much of the bolometer's spectral range. One can use bandpass filters designed for operation at 45° angles to split signal radiation into multiple channels for simultaneous observation. This ability is of great importance in airborne or space-based environments, for which observation time can be costly. In a subharmonically pumped mixer, one can use a bandpass filter to suppress fundamental mixing by blocking signal radiation near the local oscillator frequency and passing signal radiation near the Nth harmonic of the local oscillator.

A number of interesting structures with bandpass–reject characteristics have been reported in the literature, including arrays of circular[1] and square[2] conducting rings and pairs of concentric circular conducting rings.[3] Krug *et al.*[4] described arrays of annular slots and square annular slots in metal films situated on dielectric substrates. These annular arrays exhibited peak transmittances approaching 70%. We report here on freestanding resonant metal-mesh bandpass filters made up of solid copper films (typically 12-μm thick) perforated with arrays of cross-shaped apertures. Photographs of two of these devices with center frequencies at 585 GHz and 2.1 THz are shown in Fig. 1. These filters are compact, relatively easy to fabricate, coolable to liquid-helium temperatures, and exhibit high center-band transmission, narrow bandpass, and significant stop-band rejection. Their performance is determined by periodicity G, cross-member length K, and cross-member width J [Fig. 1(a)]. Design of resonant meshes is highly simplified by the fact that one can shift the filter profile by linearly scaling the dimensions G, K, and J, provided that G is smaller than the wavelength.

The theory behind this type of device can be traced back to the research of Pelton and Munk,[5] Agrawal and Imbriale,[6] and Rhoads, et al[7] on arrays of crossed dipoles on dielectric substrates referred to as frequency-selective surfaces. One can apply the physics of frequency-selective surfaces to freestanding resonant meshes by choosing the refractive index $n = 1$ (no substrate) and by applying Babinet's theorem for transformation between complementary structures.

Reports on resonant meshes were first published by Ulrich,[8] Davis,[9] and Tomaselli *et al.*[10] A theoretical description for meshes with finite thickness is given

E. R. Mueller is with the Submillimeter Technology Laboratory, University of Massachusetts at Lowell, Lowell, Massachusetts 01854; the other authors are with the Department of Electrical Engineering, University of Virginia, Charlottesville, Virginia 22903.

Received 15 October 1993; revised manuscript received 2 February 1994.

0003-6935/94/256046-07$06.00/0.

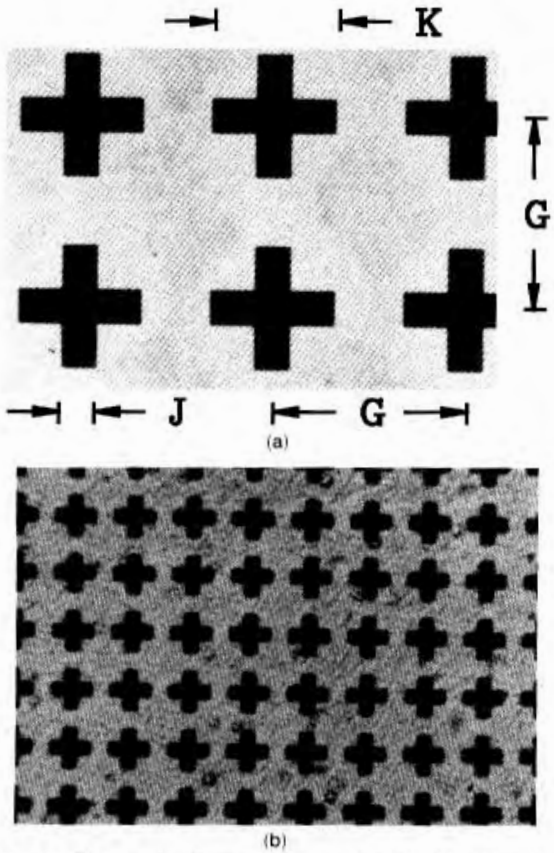

Fig. 1. Photographs of mesh filter: (a) 585 GHz (402/261/76), (b) 2.1 THz (113/73/21).

by Compton *et al.*[11] General reviews of far-infrared bandpass filters are given by Sakai and Genzel,[12] Timusk and Richards,[13] and Carniglia.[14] Filters for nonnormal incidence were fabricated by Siegel, *et al.*[15] They showed that the geometrical projection with respect to the equivalent 90° mesh nearly matches the spectrum for normal incidence. In general, the bandwidth becomes smaller as the G/K and G/J ratios are increased. The bandpass center frequency is mainly dependent on cross-member length K. It has been reported that the passband transmission of these devices tends to degrade as the center frequency is increased.[16] This degradation is believed to be caused by the increase in pattern deformity with respect to wavelength rather than a fundamental limitation. Using advanced photolithography and taking special care to maintain pattern uniformity over the entire surface, we have not observed this degradation in performance over the range of 585 GHz to 2.1 THz. Loss is due mainly to ohmic losses in the metal screen. Because individual apertures are much smaller than the wavelength of the band center, scattering and diffraction are less of a concern.

Fabrication

The fabrication process begins with the deposition of a nominal 3000-Å-thick layer of copper onto a glass plate. We then clean the copper-coated plate by using ethanol, trichloroethane, and methanol followed by a 5-min dehydration bake at 120 °C. A longer or hotter bake results in excessive oxidation of the copper. The plate is then given a 10-min Shipley hexamethyldisilizane vapor phase exposure. We apply a nominal 6- to 12-μm layer of photoresist by spinning Hoechst Celanese AZP4620 photoresist at 5000 rpm for 60 s. The plate is then soft baked at 120 °C for 60 s and allowed to cool for 10 min. A 40-s exposure to near ultraviolet is followed by 2.5-min development consisting of four parts de-ionized water and one part AZ400K Hoechst Celanese developer. The plate is then thoroughly rinsed in de-ionized water. The result is a copper-coated plate covered with an array of 6- to 12-μm thick crosses made of photoresist. Pattern uniformity and vertical sidewalls are essential.

The plate is then deoxidized in a 10% solution of H_2SO_4 followed by a short alkaline cleaning. A nominal 12-μm layer of copper is then electroplated to the surface surrounding the raised photoresist crosses. The resultant copper mesh is then gently peeled from the glass plate. Application of ultrasound in an acetone bath helps promote the peeling process and also removes the photoresist from the mesh wells. Our last step is to remove the initial 3000-Å copper layer with a short dip in a wet copper etch.

Results

Transmission

We performed Fourier transform spectroscopy to characterize the spectral response of the filters. The spectral data of Fig. 2 was taken on a Digilab FTS80 Fourier transform spectrometer (FTS), with the spectral resolution set to 7.5 GHz. The beam splitter used in the FTS caused significant data corruption in a small frequency band between 1.3 and 1.4 THz. Within this band, the corrupted data were replaced by

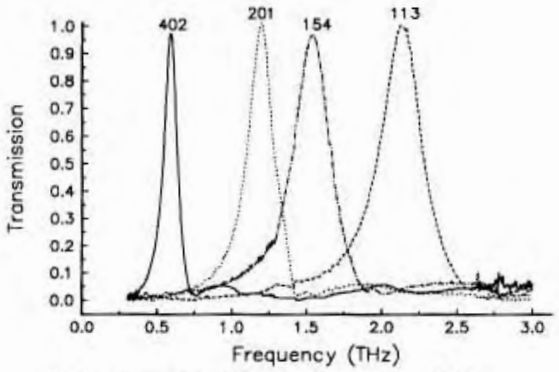

Fig. 2. Spectral profiles of four bandpass mesh filters.

Table 1. Design and Measured Mesh Filter Characteristics

$G/K/J$ (μm)	Frequency f_D (THz)	Frequency f_P (THz)	Transmission t_D	Transmission t_P	$\Delta f_{3dB}/f_P$ (%)	$\Delta f_{10dB}/f_P$ (%)
402/261/76 (402/251/66)[a]	0.585	0.587	0.97	0.97	17.3	43.1
201/131/38 (201/126/33)[a]	1.170	1.195	0.95	1.00	16.9	43.1
154/100/29 (154/98/28)[a]	1.523	1.537	0.96	0.97	18.6	49.4
113/73/21 (113/71/19)[a]	2.084	2.125	0.93	1.00	15.0	41.7

[a] $(G/K/J)$ indicates mesh dimensions as measured with a calibrated microscope.

a straight-line interpolation. Although the FTS chamber is evacuated, the ~3 cm of atmosphere between the FTS output window and the liquid-helium-cooled bolometer causes measurement errors near strong water lines. Consequently, a peak transmission of 101% was measured for the 1.17-THz bandpass filter. We determined the accuracy of the FTS data by examining the ratio of two successive background spectra. The resulting ratio was 100% ± 1%, indicating 1% accuracy. During the FTS measurements, the mesh filters were aligned so that incident radiation was nearly normal to the plane of the mesh (nominally 2° from normal).

Table 1 summarizes the physical and spectral characteristics of the mesh filters, including design dimensions $G/K/J$, design center frequency f_D, measured peak transmission frequency f_P, power transmission at the design frequency t_D, and power transmission at the peak t_P. The 3- and 10-dB bandwidths expressed as a percentage of the peak frequency ($\Delta f_{3dB}/f_P$, $\Delta f_{10dB}/f_P$) are also shown in Table 1. Dimensions $G/K/J$ are given for the production photomasks and the resultant meshes. Microscope measurement errors for G, K, and J were estimated to be no worse than ±1%.

As we see from the data, the FTS measurements showed extremely high center-band transmission. To confirm the FTS results independently, we performed a second test at 585 GHz by using a bolometer and a far-infrared laser. The insertion of the 585-GHz bandpass filter into the laser radiation path resulted in a nominal 2–3% reduction in the bolometer reading. This was in good agreement with the FTS result of 97% transmission for this filter. To confirm the expected polarization independence of the meshes, we propagated a 585-GHz far-infrared laser beam through the filter for various angles of rotation of the filter about its normal axis. No noticeable change in transmission was observed.

We also used the heterodyne receiver shown in Fig. 3 to verify the FTS data at 585 GHz. Blackbody radiation from a liquid-nitrogen bath at 77 K and a 290 K body were alternately directed to an input port of a Martin–Puplett diplexer[17] by means of a gold-mirrored chopper blade. The chopped radiation was

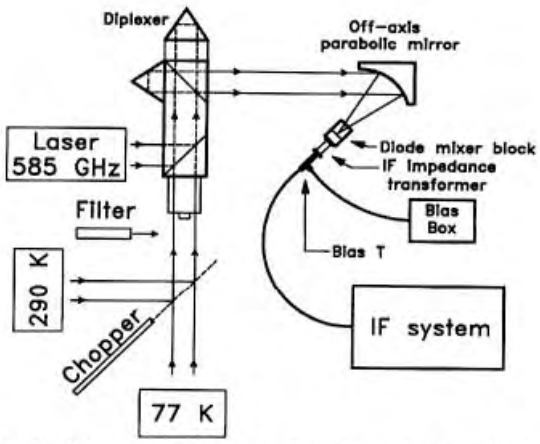

Fig. 3. Filter transmission test configuration employing a submillimeter wave mixer; IF, intermediate frequency.

spatially overlapped with 585-GHz laser radiation by the diplexer. The spatially overlapped radiation was focused onto a Schottky diode mixer in a corner cube by an off-axis parabolic mirror. We measured the 585-GHz laser radiation to be nominally 1 mW, and we used it as a local oscillator to pump the mixer. A receiver noise temperature (T_{rec}) of 3280 K double sideband was measured through the use of the Y-factor method.[18] A 585-GHz bandpass mesh filter was inserted into the blackbody radiation path, and the receiver noise temperature (T_{rec}') rose to 3415 K double sideband.

Modeling the mesh filter as an attenuator with loss L_f operating at an ambient temperature T_0 = 290 K, we see that T_{rec}' is given by

$$T_{rec}' = (L_f - 1)T_0 + L_f T_{rec}. \quad (1)$$

Inserting the measured values, we find that Eq. (1) yields L_f = 1.037 or a transmission of 96.4%, again in excellent agreement with the FTS measurements. Alternatively, the filter could be assumed to be a lossless element with transmission (t) and reflection (r), where $t = T_{rec}/T_{rec}'$. Inserting the measured values results in a filter transmission of 96%, which is also in good agreement with the FTS data.

Diffraction

We used a bolometer with a 2-mm aperture and a noise equivalent power of 2×10^{-13} W/Hz$^{1/2}$ in conjunction with a computer-controlled translation stage to map slices through the Gaussian beam of a far-infrared laser operating at 585 GHz. A 1-mm step size was used in the bolometer translation, and a lock-in amplifier was utilized for improved sensitivity. The solid curve in Fig. 4 is the result of a slice taken without a filter in the beam path. A second slice was taken with the 585-GHz filter (402/261/76) in the beam path. The resulting data are plotted in Fig. 4 as individual, unconnected data points. The same

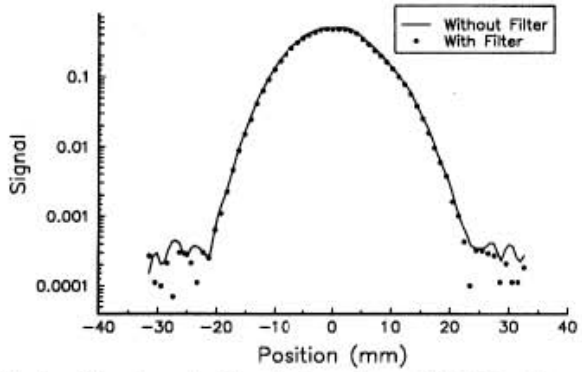

Fig. 4. Slices through a Gaussian laser beam at 585 GHz, with or without a mesh filter in the beam path.

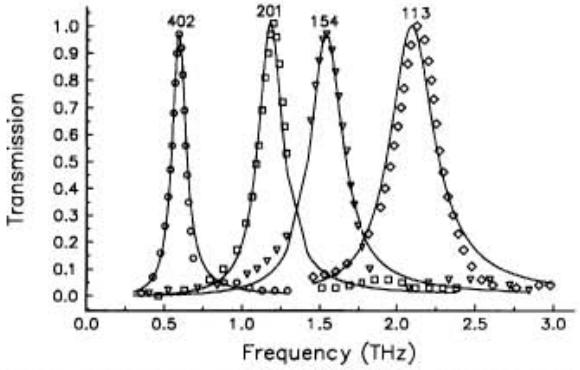

Fig. 6. Modeled data (curves) and measured FTS data (data points) for four mesh filters. The model used is that of Fig. 5 with R, L, and C values fitted to the FTS data for the 585-GHz mesh filter and then scaled for the higher-frequency filters.

normalization constant was used for both slices. As shown in Fig. 4, the data from the two slices overlap to at least 35 dB down, the dynamic range noise floor of the lock-in amplifier. It is apparent from this graph that the beam profile is essentially unaltered by the insertion of the mesh filter.

Scaling–Modeling

The initial 585-GHz filter photomask design was based on theoretical considerations. We then analyzed the resultant filter spectrum to determine the actual center frequency. Using these data, we slightly adjusted the photomask dimensions to obtain a filter centered at 585 GHz. The remaining filters were scaled directly from the final 585-GHz filter dimensions (all dimensions were rounded to the nearest micrometer). The resultant peak frequencies were all within 2% of the design frequencies, confirming the theoretically predicted scaling characteristic of these devices.

We used the simple circuit shown in Fig. 5 to model the mesh filters. The circuit is based on the model used by Davis.[9] Transmission lines with the characteristic impedance of free space provide a means to propagate electromagnetic energy to and from the filter. The load resistance, R_L, and the source resistance, R_S, are matched to the characteristic impedance of the transmission lines ($Z_0 = 377\ \Omega$) so that standing waves are avoided. Capacitor C and inductor L set the resonant frequency [$\omega_r = (LC)^{-1/2}$], and resistor R models ohmic losses in the mesh. In the case of very small ohmic loss, a condition satisfied for

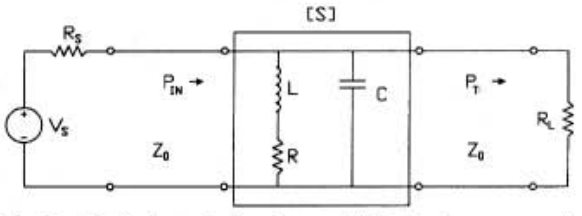

Fig. 5. Simple transmission line model for bandpass resonant mesh filters.

transmission peaks in excess of 97%, quality factor Q of the circuit is given approximately as $Q = \omega_r C Z_0/2$, and the fractional bandwidth is approximately given as $1/Q$. Under the matched conditions $R_L = R_S = Z_0$, the power transmission of the circuit is given by

$$\frac{P_T}{P_{IN}} = |S_{21}|^2 = 1 - \left[\frac{|(Z_{grid}|Z_0) - Z_0|}{|(Z_{grid}|Z_0) + Z_0|}\right]^2, \qquad (2)$$

with $Z_{grid} = (R + j\omega L)\|(j\omega C)^{-1}$.

We found values of $R = 7.8 \times 10^{-2}\ \Omega$, $L = 8.345$ pH, and $C = 8.782$ fF for the 585-GHz model by matching the FTS data of the 585-GHz mesh filter to the relevant circuit equations. We scaled the L and C values of the 585-GHz model to obtain inductor and capacitor values for the remaining filters. Resistor values were not scaled in this manner; instead we calculated them to give peak power transmission equal to the FTS data for each filter. It is not in the least surprising that the resonant frequency scaled accurately, but it is notable that the bandwidth of the scaled models closely matched the measured bandwidths. It is apparent from the transmission curves of Fig. 6 that this model can fairly accurately predict mesh filter performance provided that the G/K and G/J ratios are maintained. However, it is desirable for us to have a modeling method that can predict performance for arbitrary G/K and G/J ratios or other arbitrary aperture geometries.

Two other modeling methods were explored that predict the mesh filter performance from first principles. The two models were the finite-element method and the EMF analysis. Both methods assume an infinite mesh array and utilize symmetries to reduce the structure to a single unit cell defined by electric and magnetic walls. The structure shown in Fig. 7 represents a single element of the metal-mesh filter embedded in a waveguide. Evanescent modes around the metal-mesh unit cell act as reactances in the waveguide.

Hewlett-Packard's high-frequency structure simulator (HFSS) solves Maxwell's equations on arbitrary

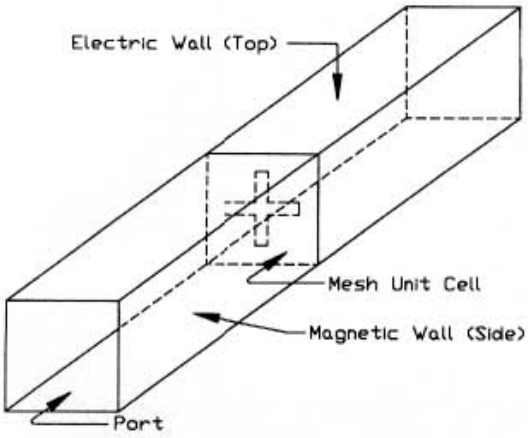

Fig. 7. Mesh filter unit cell embedded in a waveguide with electric walls on the top and bottom and magnetic walls on both sides.

three-dimensional structures composed of lossy metals, dielectric materials, and perfect conductors by using the finite-element technique and determines reflection and transmission coefficients.[19] We used the HFSS to obtain the two port $[s]$ parameters of the mesh over a wide range of frequencies centered at the resonant frequency of the mesh. We used only one quarter of the symmetric structure of Fig. 7 in the HFSS simulations to reduce the solve time. Figure 8 shows the HFSS solution and the FTS measurement for the 585-GHz and 2.1-THz filters. The HFSS model peak frequency for both filters was within 1.5% of the measured FTS transmission peak frequencies. The percentage bandwidth for both filters was predicted by HFSS to within 4% of the measured FTS percentage bandwidth. In addition, the HFSS percentage bandwidth decreased with frequency from 14.5% at 585 GHz to 11% at 2.1 THz, which agrees with the trend of the experimental FTS data. We believe that differences between the measured FTS data and the modeled HFSS data are attributable to small errors in the measurement of the mesh dimensions, slight imperfections in the apertures, and the assumption of an infinite mesh array.

The main disadvantages of using the HFSS are the large amount of computer resources required for a solution and the high cost of the software. We explored the EMF method because of its relatively simple implementation compared with either the finite-element method of the HFSS or the Floquet mode-expansion technique. The induced EMF method starts by assuming a current distribution on the structure being modeled. Once these currents are given, the method uses Poynting's theorem to find an expression for the impedances of the structure in the waveguide. The structure shown in Fig. 9, one quarter of the mesh unit cell, is the dual of the post in a waveguide solved by Eisenhart and Khan, and the derivation of the impedances follows a similar procedure.[20,21] We assumed that magnetic currents in the cross arm perpendicular to M were negligible. The effect of adding in the cross arm is to reduce the distributed capacitance along the intersecting area

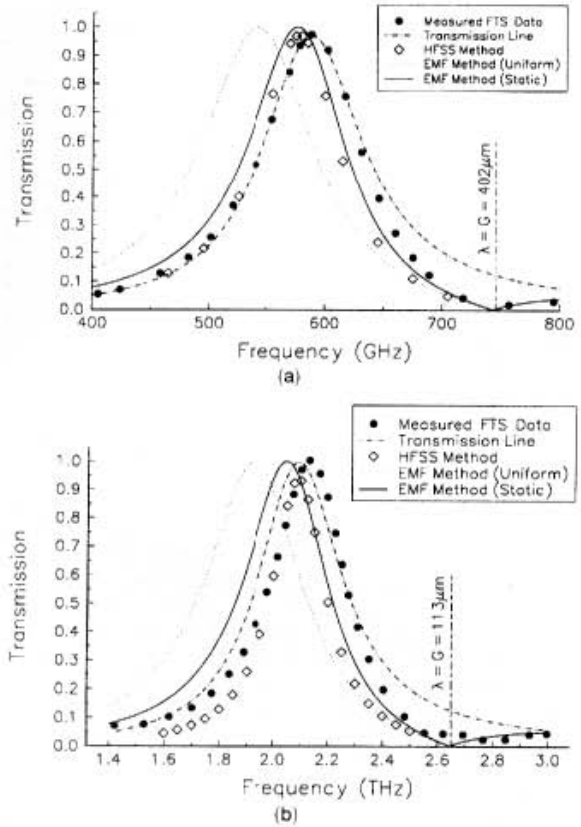

Fig. 8. Measured and modeled transmission for the (a) 585-GHz mesh filter, (b) 2.1-THz mesh filter; transmission line curves are the same as the ones shown in Fig. 6.

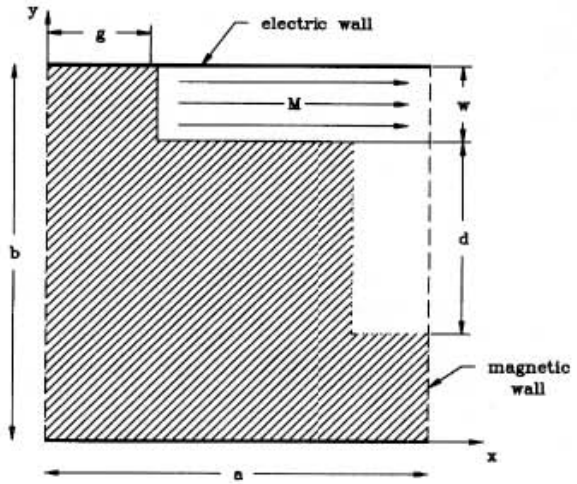

Fig. 9. Unit cell used in the EMF method, where M is the assumed magnetic current distribution in the aperture.

between the two arms, thus reducing the overall capacitance by a geometrical factor of approximately $\zeta_{geom} = d/(d + w)$. The equations for the circuit elements derived from this method are given by

$$C_0 = \zeta_{geom} \frac{1}{j\omega} \frac{2a}{b} \sum_{n=1}^{\infty} \gamma_{y,n}{}^2 (Y_{0n}{}^{TM+} + Y_{0n}{}^{TM-}), \quad (3)$$

$$C_m = \frac{1}{j\omega} \frac{a}{2b} \frac{1}{\gamma_{x,m}{}^2} \sum_{n=0}^{\infty} \frac{\varepsilon_{0n}}{k_x{}^2 + k_y{}^2} \times \gamma_{y,n}{}^2 k_y{}^2 (Y_{mn}{}^{TM+} + Y_{mn}{}^{TM-}), \quad (4)$$

$$L_m{}^{-1} = j\omega \frac{a}{2b} \frac{1}{\gamma_{x,m}{}^2} \sum_{n=0}^{\infty} \frac{\varepsilon_{0n}}{k_x{}^2 + k_y{}^2} \times \gamma_{y,n}{}^2 k_x{}^2 (Y_{mn}{}^{TE+} + Y_{mn}{}^{TE-}), \quad (5)$$

where $k_x = m\pi/a$, $k_y = n\pi/b$, and ε_{0n} is the Neumann factor given by

$$\varepsilon_{0n} = \begin{cases} 2, & n = 0 \\ 1, & n \neq 0 \end{cases}. \quad (6)$$

Factors $Y_{mn}{}^{TM}$ and $Y_{mn}{}^{TE}$ are the characteristic admittances for the waveguide modes (plus or minus superscripts indicate the impedances looking in the positive and negative z directions, respectively), given by

$$Y_{mn}{}^{TM} = \frac{\omega\varepsilon}{k_z}, \quad (7)$$

$$Y_{mn}{}^{TE} = \frac{k_z}{\omega\mu}, \quad (8)$$

where k_z is the mode propagation constant

$$k_z = (\omega^2\mu\varepsilon - k_x{}^2 - k_y{}^2)^{1/2}. \quad (9)$$

The terms $\gamma_{x,m}$ and $\gamma_{y,n}$ are dependent on the assumed current distribution. For a uniform current distribution across the aperture,

$$\gamma_{x,m} = \operatorname{sinc}\left(\frac{m\pi g}{a}\right), \qquad \gamma_{y,m} = \operatorname{sinc}\left(\frac{n\pi w}{b}\right). \quad (10)$$

We also looked at a more accurate current distribution with singularities at the aperture edges. This distribution was based on the assumption that magnetic currents in the aperture have the same spatial distribution as static charges on an infinitely long strip of metal. The current distribution in the aperture is then given by

$$\mathbf{M}_a = \frac{M_o}{[w^2 - (b - y)^2]^{1/2}} \hat{x}. \quad (11)$$

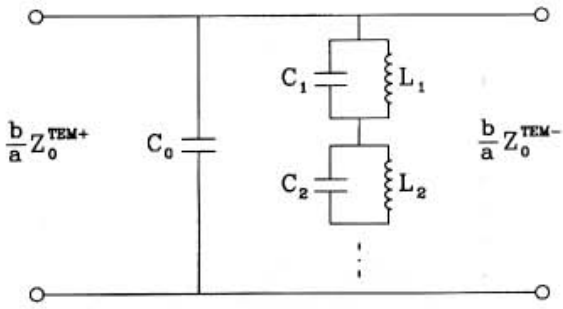

Fig. 10. Transmission line model derived from the EMF method.

Using the nonuniform current distribution, we found $\gamma_{x,m}$ and $\gamma_{y,n}$ to be

$$\gamma_{x,m} = \frac{2}{\pi} \int_0^g \left[\frac{\cos\left(\frac{m\pi x}{a}\right)}{(g^2 - x^2)^{1/2}} \right] dx,$$

$$\gamma_{y,n} = \frac{2}{\pi} \int_0^w \left[\frac{\cos\left(\frac{n\pi y}{b}\right)}{(w^2 - y^2)^{1/2}} \right] dy. \quad (12)$$

The circuit model resulting from the EMF formulation is shown in Fig. 10. We use the impedances calculated from Eqs. (3)–(5) with Eq. (2) to calculate the transmission characteristics of the mesh [we truncated Eqs. (3)–(5) at $m = n = 50$]. Figure 8 shows the results of the EMF method for both the uniform and nonuniform magnetic current distributions. The assumption of a uniform current distribution caused the EMF method to overestimate the grid impedance. The EMF method with the nonuniform current distribution estimated the peak frequency for both filters to within 4% of the measured FTS transmission peak frequencies and estimated the percentage bandwidth for both filters to within 3% of the measured FTS percentage bandwidth. A limitation to the EMF method is that the structure must be simple enough so that the current distribution can be approximated with reasonable accuracy.

Conclusion

Bandpass filters for the submillimeter wave range with center-frequency power transmission ranging from 97 to 100% have been fabricated. The power transmission for one of the filters has been measured with three independent methods. Corresponding stop-band rejection in excess of 18 dB has been achieved, and the filters exhibited no noticeable diffraction effects. We believe the enhanced performance over previous results is due to an increase in pattern uniformity resulting from improved photolithography. The ability to shift a filter's spectral profile through simple scaling of the mesh dimensions was demonstrated to within a 2% margin of error.

An *RLC* circuit embedded in a transmission line was shown to provide a simple and fairly accurate model for predicting mesh filter performance. We based R, L, and C values on FTS measurements of a previously fabricated 585-GHz mesh. The circuit elements were shown to scale accurately with frequency and mesh dimensions so that mesh filter performance could be predicted as long as the G/K and G/J ratios were maintained. To overcome this limitation we used Hewlett-Packard's HFSS to solve Maxwell's equations over a single mesh element and to obtain two port $[s]$ parameters for an infinite mesh. The HFSS also has the advantage of being able to determine the electromagnetic properties of meshes with arbitrarily shaped mesh elements. The induced EMF method provides a closed-form mathematical formulation that can be used to predict the performance of meshes with cross-shaped apertures. This method provides fairly accurate results for structures in which a reasonable guess for the magnetic current distribution can be made. The EMF method is less expensive and easier to implement than the more cumbersome finite-element and Floquet mode-expansion techniques.

The authors gratefully acknowledge the efforts of H. P. Röser and G. Lundershausen of the Max Planck Institute for Radioastronomy in Bonn. Their assistance was critical to the fabrication process. This research was supported by the U.S. Army under contract DAHC90-91-C-0030.

References

1. E. A. Parker and S. M. A. Hamdy, "Rings as elements for frequency selective surfaces," Electron. Lett. **17,** 612–614 (1981).
2. K. J. Kogler and R. G. Pastor, "Infrared filters fabricated from submicron loop antenna arrays," Appl. Opt. **27,** 18–19 (1988).
3. E. A. Parker, S. M. A. Hamdy, and R. J. Langley, "Arrays of concentric rings as frequency selective surfaces," Electron. Lett. **17,** 880–881 (1981).
4. P. A. Krug, D. H. Dawes, R. C. McPhedran, W. Wright, J. C. Macfarlane, and L. B. Whitbourn, "Annular-slot arrays as far-infrared bandpass filters," Opt. Lett. **14,** 931–933 (1989).
5. E. L. Pelton and B. A. Munk, "Scattering from periodic arrays of crossed dipoles," IEEE Trans. Antennas Propag. **AP-27,** 323–330 (1979).
6. V. D. Agrawal and W. A. Imbriale, "Design of a dichroic Cassegrain subreflector," IEEE Trans. Antennas Propag. **AP-27,** 466–473 (1979).
7. C. M. Rhoads, E. K. Damon, and B. A. Munk, "Mid-infrared filters using conducting elements," Appl. Opt. **21,** 2814–2816 (1982).
8. R. Ulrich, "Interference filters for the far infrared," Appl. Opt. **7,** 1987–1996 (1968).
9. J. E. Davis, "Bandpass interference filters for very far infrared astronomy," Infrared Phys. **20,** 287–290 (1980).
10. P. Tomaselli, D. C. Edewaard, P. Gillan, and K. D. Möller, "Far-infrared bandpass filters from cross-shaped grids," Appl. Opt. **20,** 1361–1366 (1981).
11. R. C. Compton, R. C. McPhedran, G. H. Derrick, and L. C. Botten, "Diffraction properties of a bandpass grid," Infrared Phys. **23,** 239–245 (1983).
12. K. Sakai and L. Genzel, *Review of Millimeter Waves* (Plenum, New York, 1983), Vol. 1, pp. 155–247.
13. T. Timusk and P. L. Richards, "Near millimeter wave bandpass filters," Appl. Opt. **20,** 1355–1360 (1981).
14. C. K. Carniglia, "Comparison of several shortwave pass filter designs," Appl. Opt. **28,** 2820–2823 (1989).
15. P. H. Siegel, R. J. Dengler, and J. C. Chen, "THz dichroic plates for use at high angles of incidence," IEEE Microwave Guided Wave Lett. **1,** 8–9 (1991).
16. S. T. Chase and R. D. Joseph, "Resonant array bandpass filters for the far infrared," Appl. Opt. **22,** 1775–1779 (1983).
17. D. H. Martin, *Polarizing (Martin–Puplett) Interferometric Spectrometers for the Near- and Submillimeter Spectra*, Vol. 6 of Infrared and Millimeter Waves, K. J. Button, ed. (Academic, New York, 1982).
18. D. M. Pozar, *Microwave Engineering* (Addison-Wesley Reading, Mass., 1990), pp. 594–602.
19. *HFSS User's Reference Manual* (Hewlett-Packard, Santa Rosa, Calif.), App. A.
20. R. L. Eisenhart and P. J. Khan, "Theoretical and experimental analysis of a waveguide mounting structure," IEEE Trans. Microwave Theory Tech. **MTT-19,** 706–719 (1971).
21. D. B. Rutledge and S. E. Schwarz, "Planar multimode detector arrays for infrared and millimeter-wave applications," IEEE J. Quantum Electron. **QE-17,** 407–414 (1981).